ARTICLES
PUBLISHED ONLINE: 27 JULY 2015 | DOI: 10.1038/NNANO.2015.149
nature nanotechnology

A monolithic white laser

Fan Fan[1†], Sunay Turkdogan[1†], Zhicheng Liu[1†], David Shelhammer[1] and C. Z. Ning[1,2*]

Monolithic semiconductor lasers capable of emitting over the full visible-colour spectrum have a wide range of important applications, such as solid-state lighting, full-colour displays, visible colour communications and multi-colour fluorescence sensing. The ultimate form of such a light source would be a monolithic white laser. However, realizing such a device has been challenging because of intrinsic difficulties in achieving epitaxial growth of the mismatched materials required for different colour emission. Here, we demonstrate a monolithic multi-segment semiconductor nanosheet based on a quaternary alloy of ZnCdSSe that simultaneously lases in the red, green and blue. This is made possible by a novel nanomaterial growth strategy that enables separate control of the composition, morphology and therefore bandgaps of the segments. Our nanolaser can be dynamically tuned to emit over the full visible-colour range, covering 70% more perceptible colours than the most commonly used illuminants.

Multi-colour or multi-wavelength lasers with a wavelength span beyond the capability of a single laser material have been a subject of great interest in recent years[1–9], with the realization of white lasers as the ultimate goal. In fact, lasers that span the full visible spectrum, particularly the red, green and blue (RGB) colours, are particularly useful for laser lighting[10,11], full-colour laser imaging and display[12,13], biological and chemical sensing[14,15], as well as on-chip wavelength-division multiplexing[16,17]. As an illuminant, lasers offer higher energy conversion efficiencies and potentially higher output powers than white light-emitting diodes (LEDs) and other traditional illuminants. It has recently been demonstrated that illumination with four monochromatic lasers is visually equivalent to a continuous-spectrum white reference illuminant as seen by the human eye[10,11]. Furthermore, the highly monochromatic component colours allow for a wider achievable colour gamut (more than 90% of all colours perceptible to human eyes), a higher contrast ratio and more vivid colours than traditional display systems based on broadband light sources (Supplementary Section 12).

Despite the great efforts made to achieve multi-colour lasing using a variety of approaches, a single monolithic semiconductor laser capable of lasing with all three elementary colours has not yet been realized due to several significant challenges. First, most of the previous approaches use non-semiconductor materials such as nonlinear optical crystals[3], rare-earth doped materials[4], dye-doped polymers[5] or liquids[6], or microfibres[7]. Such set-ups are bulky, inefficient and incompatible with electrical injection, an important ultimate requirement for many applications. Second, semiconductor-based approaches[7,9] combine several discrete devices in a heterogeneous manner, thus increasing the volume, complexity and cost of the overall system. Producing emission covering all visible wavelengths in a single structure requires the growth of potentially very dissimilar semiconductors into a monolithic structure with high crystal quality. This has been a goal pursued by the crystal growth community for decades and remains a challenging one, especially using conventional planar epitaxy techniques, because of the large lattice mismatch involved. As an alternative to standard planar epitaxial structures, developments in nanotechnology over the last two decades have demonstrated the use of quantum dots[18] and nanowires[19–21] as means of producing emission in a wide spectral range, but serious issues remain. For quantum dots made with solution-based techniques[2], control of their spatial distribution to avoid the absorption of short wavelength emission by narrow-gap dots remains difficult. More importantly, electrical injection remains a fundamental challenge for lasers, despite successful demonstrations of full-colour LEDs[22,23]. Beyond material growth, it is also critically important to realize a growth-compatible cavity structure in which the lasing of all three elementary colours can be supported simultaneously, while minimizing absorption of the short-wavelength emission by narrow-gap materials.

In our efforts to achieve such an ultimate goal, we have already demonstrated two-colour lasing[24,25] from a single two-segment CdSSe nanosheet[24,26] and from a nanowire with a looped end[25]. We determined that two-colour lasing from a monolithic structure could best be achieved using a side-by-side cavity geometry (Supplementary Sections 1–4) rather than a longitudinal heterostructure, due to the absorption of short-wavelength emission by narrow-gap material. However, adding a third segment capable of blue lasing to ultimately enable white lasing was challenging. ZnS is the most compatible material and an ideal candidate to add into the ternary CdSSe alloy. It is known to alloy in various combinations with Cd, S and Se, and it would extend the bandgap to allow blue emission. Unfortunately, due to the low vapour pressure and low supersaturation of ZnS[27], such ZnS-dominant alloys typically grow into nanowires or nanoribbons with very high length–width aspect ratios[28–30]. This is why, to date, ultraviolet and blue lasing in this material system has only been demonstrated in nanowires[31] and nanoribbons[32] with high aspect ratios (>20). Such structures are intrinsically incompatible with the low-aspect-ratio nanosheet morphology of CdS and CdSe required to achieve simultaneous green and red lasing (Supplementary Section 4).

In this Article we report a monolithic semiconductor white laser. To overcome the fundamental challenges to obtain the required materials and structures for white lasing, we have made systematic efforts to understand and control the interplay of various growth mechanisms, including the vapour–liquid–solid (VLS) and vapour–solid (VS) mechanisms, and a novel gas-phase dual-ion exchange process. This has led to the successful growth of multi-segment heterostructure nanosheets of ZnCdSSe alloys with the appropriate compositions, cavity geometries and aspect ratios to emit red, green and blue light simultaneously. These multi-segment structures were achieved by using a highly coordinated,

[1]School of Electrical, Computer and Energy Engineering, Arizona State University, Tempe, Arizona 85287, USA. [2]Department of Electronic Engineering, Tsinghua University, Beijing, China. †These authors contributed equally to this work. *e-mail: cning@asu.edu

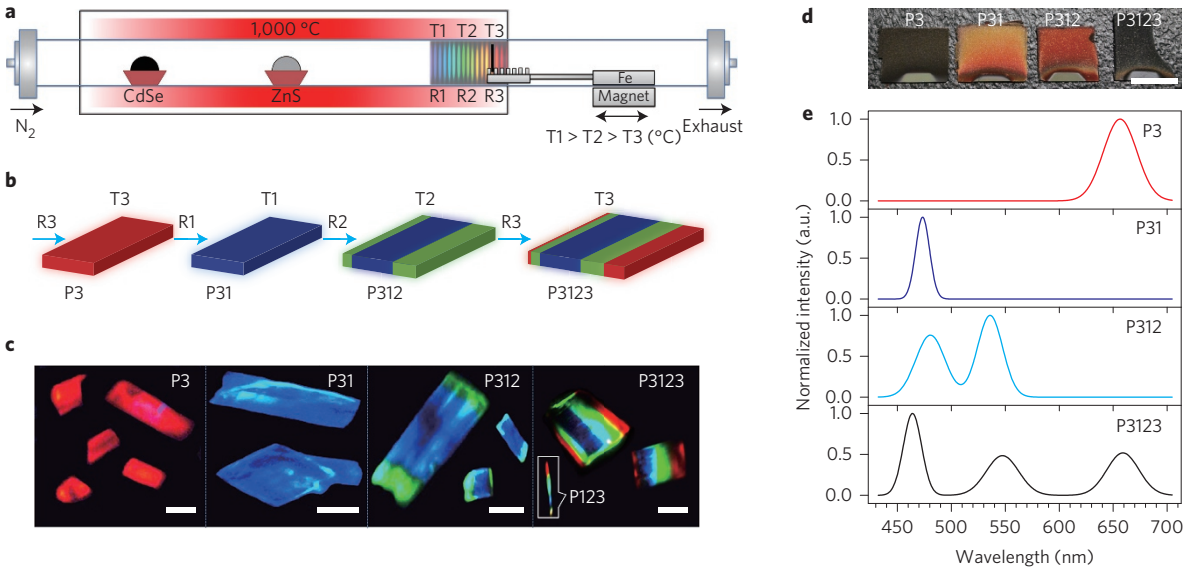

Figure 1 | Growth procedure of multi-segment heterostructure nanosheets. a, Schematic of the CVD set-up with a temperature gradient of 66 °C cm^{-1} in the region used for positioning the substrate (see Supplementary Section 5 for more details). **b**, Illustration of the growth procedure. Samples are grown starting at position R3, then at positions R1, R2 and finally back to R3, with corresponding temperatures labelled T1, T2 and T3. The associated product samples after these steps are labelled P3, P31, P312 and P3123, respectively, where the numbers following 'P' represent the growth sequence at various locations. For example, P312 represents a product grown first at R3, followed by growths at R1 and then at R2. **c**, Photoluminescence images of individual structures after the corresponding growth sequences. Note that the images were taken after the structures were transferred onto a glass substrate from their as-grown ones using a contact printing method. Inset in rightmost panel a multi-segment nanowire structure resulting from the P123 growth sequence. Scale bars, 15 μm. **d**, Optical images of the samples under ambient lighting. Scale bar, 1 cm. **e**, Photoluminescence spectra of the samples shown in **c**,**d**.

dynamical positioning of the substrates and switching of precursors during growth. Rather than attempt to directly grow a ZnS-rich segment next to the CdS- and CdSe-rich segments, we optimized the growth sequence and conditions such that CdSe nanosheet growth was followed by a dual-ion exchange reaction, a mechanism that has not been reported previously, to finally achieve a ZnS-rich nanosheet structure. By independently controlling the optical pumping power to each segment we demonstrate full-colour tunable lasing over the entire triangular colour gamut, and white colour lasing in particular. The wavelength spans 191 nm and is the largest ever reported for a monolithic structure.

Growth of monolithic multi-segment heterostructure

Our multi-segment heterostructure was grown by chemical vapour deposition (CVD) (see Methods). Temperature-dependent composition control was used in the growth of the alloy semiconductors[21,32–34]. The essence of this technique is to manipulate the position of the substrate along the axial temperature gradient (Supplementary Fig. 6) in the reactor to optimize the substrate temperature for the desired alloy composition. Direct growth of the desired morphologies (such as segmented nanosheets with low aspect ratios) with the desired compositions is not possible, especially for wide-gap materials. Our strategy was to decouple the realization of the desired morphology and composition by achieving them separately, indirectly. More specifically, we obtained the desired nanosheet morphologies using materials amenable to growing with the desired morphology. Subsequent growth was performed to obtain the desired alloy composition through cation or anion exchange[35–38], without significant modification of the initial morphology. Through this highly non-equilibrium exchange process, the desired material composition–morphology combination could be achieved. Such an indirect route to achieve the desired morphologies and compositions separately can serve as a more general strategy for other materials. The morphological evolution of ZnCdSSe nanostructures as the alloy composition changes is described in Supplementary Fig. 7. Given their known alloying capabilities[33,39,40], CdSe provides an ideal template for morphology transfer to a Zn- and Se-rich ZnCdSSe alloy. It is important to note that all previous studies of substitutional reactions involved the exchange of only one of the cations or anions, but, in our case, conversion of CdSe by a ZnS source necessarily deals with the simultaneous substitution of cations and anions. Such simultaneous anion and cation exchange in the vapour phase during uninterrupted growth is crucial for the successful growth of our materials with the desired morphologies and alloy compositions (and thus bandgaps).

Consistent with common understanding[41,42], the catalyst-led VLS mechanism dominates growth at low levels of supersaturation, producing a wire-like morphology. At high supersaturation, the VS mechanism dominates growth, producing two-dimensional belts or ribbons and sheets. The optimal growth conditions are illustrated in Fig. 1 and Supplementary Fig. 6, where substrate positions R3, R2 and R1 and the corresponding temperatures are best suited for the growth of alloys with red, green and blue emission, respectively. Extensive study was carried out to determine the alloy composition and morphology at a given substrate location and temperature. Such characterization is critically important to successful control of the final morphology and alloy composition.

The growth procedure is shown schematically in Fig. 1. First, Cd- and Se-rich ZnCdSSe nanosheet structures (P3) were grown at a low temperature (at R3 with T3 ≈ 640 °C). The substrate was then moved to the higher-temperature region R1 (T1 ≈ 780 °C) using a connected iron rod driven by an external magnet to further promote diffusion processes[38]. This caused the structures to transform uniformly into a Zn- and Se-rich ZnCdSSe alloy (after P31 growth) with no appreciable change in morphology (Supplementary Section 14). Furthermore, the dual-ion exchange process does not change the wurtzite crystal and resulting crystal quality, as can be seen from the transmission electron microscopy

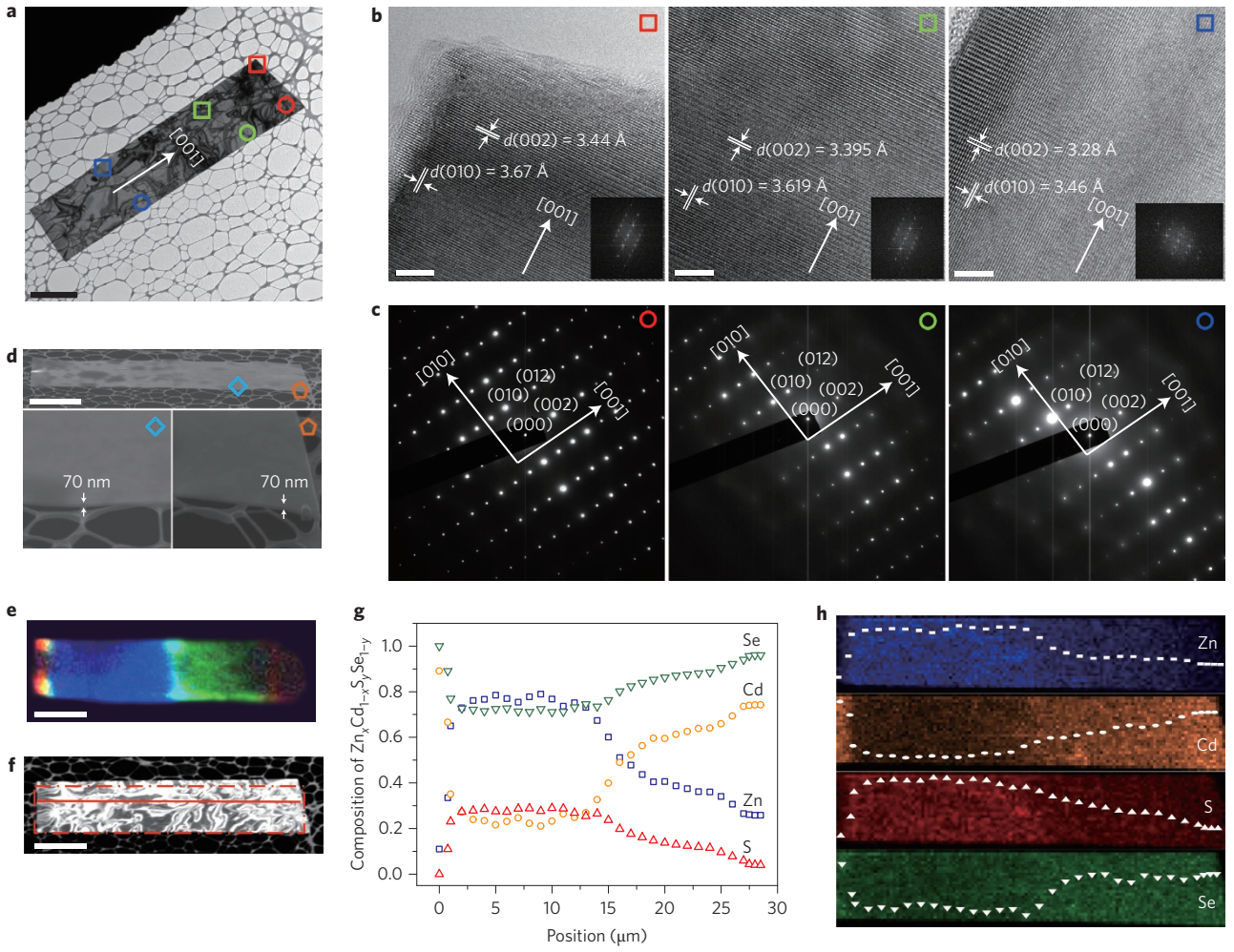

Figure 2 | Structural characterization of a multi-segment heterostructure nanosheet. a, Low-resolution TEM image of a multi-segment heterostructure nanosheet. Scale bar, 5 μm. **b**, HRTEM images of the regions inside the coloured squares in **a**, with the corresponding colour code. Scale bars, 5 nm. **c**, Indexed SAD patterns of the regions inside the corresponding coloured circles in **a**. The HRTEM images have a 30° rotation compared with the SAD patterns due to image rotation at higher magnifications. **d**, A 60° tilted SEM image of the structure with close-up views of the cross-section. The thickness was measured to be 70 nm after compensating for the tilt angle. **e**,**f**, Photoluminescence image (**e**) and scanning TEM image (**f**) of the structure. Scale bars (**d**–**f**), 5 μm. **g**, Calculated composition change along the width of the multi-segment heterostructure nanosheet based on the EDS line scan performed along the solid red line in **f**. **h**, Correlation of the EDS mapping inside the dashed rectangular area in **f**, with the atomic percentages gathered from the EDS line scan.

(TEM) and photoluminescence characterizations in Figs 2b,c and 1e, respectively. The red photoluminescence peak from P3 is entirely converted to a blue peak in P31 (Fig. 1e). The defect-free photoluminescence features in P31 indicate the high crystal quality of the transformed structures, as imperfect wide-gap semiconductors typically show strong emission below bandgaps. Based on our study, this indirect route is practically the only successful means for growing low-aspect-ratio nanosheets capable of blue emission. No combination of growth parameters could be found to produce such structures directly due to the low vapour pressures of ZnS and ZnSe. All attempts to grow wide-gap materials directly have resulted in small, multi-segment nanowires (see inset in panel 4 of Fig. 1c, indicated by P123), which are unsuitable for multi-colour lasing (Supplementary Section 1). The growth process of P31 was then followed by growth at position R2 (at T2 ≈ 740 °C) and the second segment was synthesized by incorporating more Cd ions to add green light emission (P312 in Fig. 1b). The final growth step at position R3 added the red-emitting segment, resulting in the final multi-segment heterostructure capable of simultaneous RGB light emission (P3123 in Fig. 1b). At positions R2, and later R3, the lower substrate temperatures favour the VS mechanism for two-dimensional nanosheet growth, as ion transport is dominant over the exchange processes at lower temperatures[35]. Our unique procedure relies on exploring the interplays among the VLS and VS mechanisms and the simultaneous gas-phase anion and cation exchange processes in the right sequence. By simply increasing the number of steps after the dual-ion exchange process, heterostructures can be grown with more segments, which emit more colours (any colour in the visible spectrum; see Supplementary Fig. 8 in Supplementary Section 6). More details about the growth and mechanisms are provided in Supplementary Sections 5–7.

Structural characterization

Scanning electron microscopy (SEM) images show that the structures have lengths of up to 60 μm, widths of up to 45 μm and thicknesses in the range of 60–350 nm (Fig. 2d). The high-resolution TEM (HRTEM) images and selected area diffraction (SAD) patterns in Fig. 2b and c, and the photoluminescence spectra in Fig. 1d show that each segment of the structure is a high-quality wurtzite monocrystal, with no visible defects or strains detected. Energy dispersive spectroscopy (EDS) analysis of

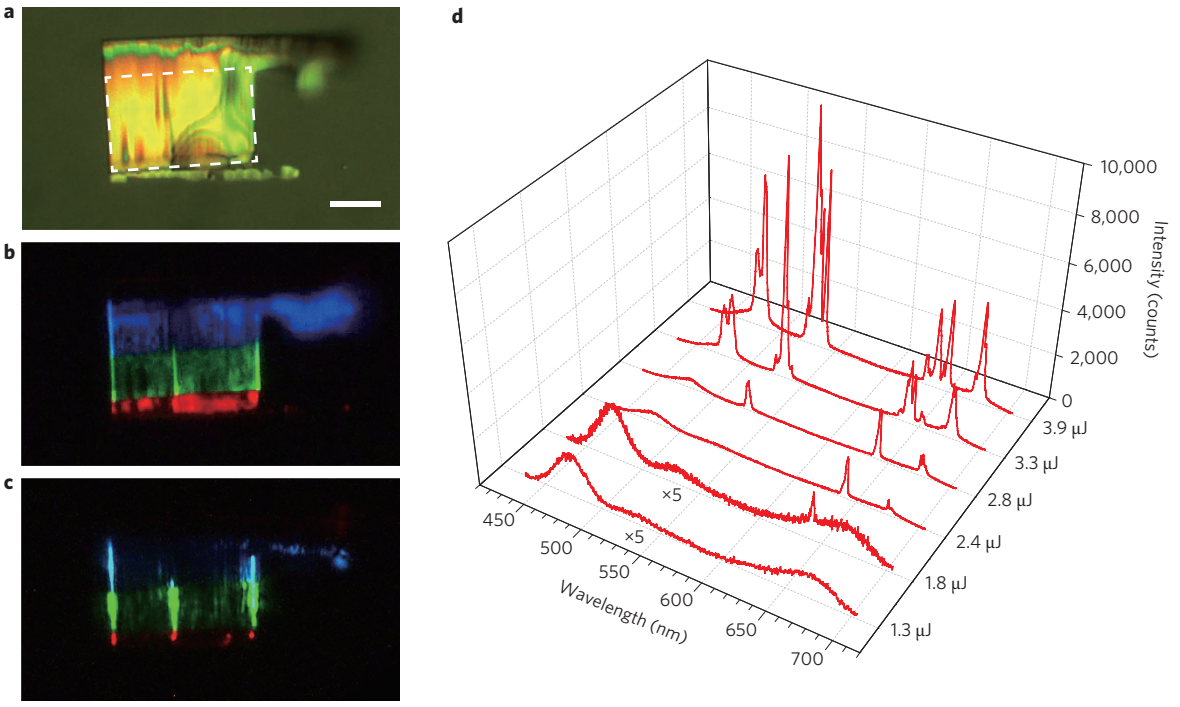

Figure 3 | Simultaneous multi-colour lasing from a single multi-segment heterostructure nanosheet. a, Bright-field optical microscope image. The dashed white box indicates the main part of the cavity. **b**,**c**, Real colour images under low (**b**) and high (**c**, above threshold) pumping of a single pumping beam (180 μm in diameter). Scale bar, 10 μm. The three strong vertical lines indicate significant scattering from the two edges and from the bent edge in the centre. **d**, Spectra at different pumping levels (as labelled on the lower right side of the figure). The intensities of the first two spectra have been multiplied by a factor of 5 to show the details.

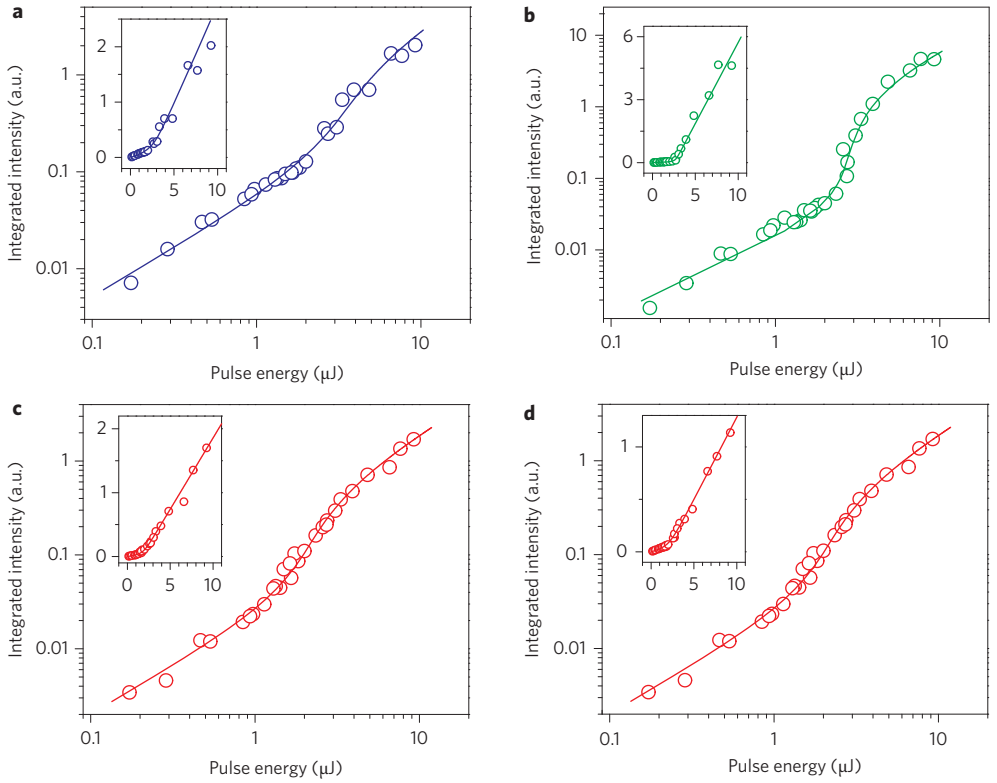

Figure 4 | Light-in–light-out curves with multimode lasing fitting. a–d, Light-in–light-out curves of the 484, 530, 642 and 675 nm lasing peaks on a log–log scale. Insets: plots on a linear scale. Circles represent direct measurements and solid lines are fits using multimode laser theory.

the representative nanosheet in Fig. 2 shows that it is composed of Zn, Cd, S and Se, and that the concentration of those elements changes along the *c* axis. As one moves from the blue-emitting towards the red-emitting region, the concentrations of Cd and Se increase while those of Zn and S decrease. Based on the EDS line scan, the (010) and (001) plane spacings and emission wavelengths along the structure were extrapolated and correlated with the measured values from the HRTEM images and photoluminescence spectra. These results are all in good agreement with those measured on a different nanosheet (Supplementary Fig. 10 in Supplementary Section 8). An EDS line scan and elemental mapping of the structure (Fig. 2g,h) show that the relative abundance of anions does not change as much as that of cations during the ion exchange process, assuming that the Zn- and Se-rich segment had approximately the same composition as the Cd- and Se-rich segment due to the identical growth conditions. This implies that the cation exchange process is faster than the anion exchange process, which would be expected due to the inhibited diffusion of the larger anions[36] (see Supplementary Section 14 for a more detail comparison). More details of the structural characterization can be found in the Methods.

Multi-colour lasing

An extensive optical study was conducted to demonstrate lasing behaviour, including the polarization dependence of the pump lasers (Supplementary Section 18). The multi-segment heterostructure nanosheets were excited by a 355 nm pulsed laser (pulse width of 9 ns). Details of the pumping and collecting configuration are provided in the Methods and in Supplementary Section 9. Figure 3 shows simultaneous multi-colour lasing behaviour from a representative sample under uniform pumping after being transferred onto an MgF_2 substrate. This sample was intentionally cleaved from a longer piece by the bend-to-fracture method[43] to create a high-quality reflecting end facet. The main part of the multi-colour lasing cavity (enclosed by the white dashed box in Fig. 3a) had dimensions of 28.0 μm × 18.0 μm × 0.3 μm. This particular nanosheet also featured narrow protruding segments of irregular shape extending to the right side of the white box, indicating that this nanosheet was imperfectly detached from a larger nanosheet (for a detailed study of the sizes and uniformity of our material, see Supplementary Section 16). Figure 3b presents a photoluminescence image under single pulse pumping at 1.2 μJ. Largely uniform spontaneous emission can be seen, with strong

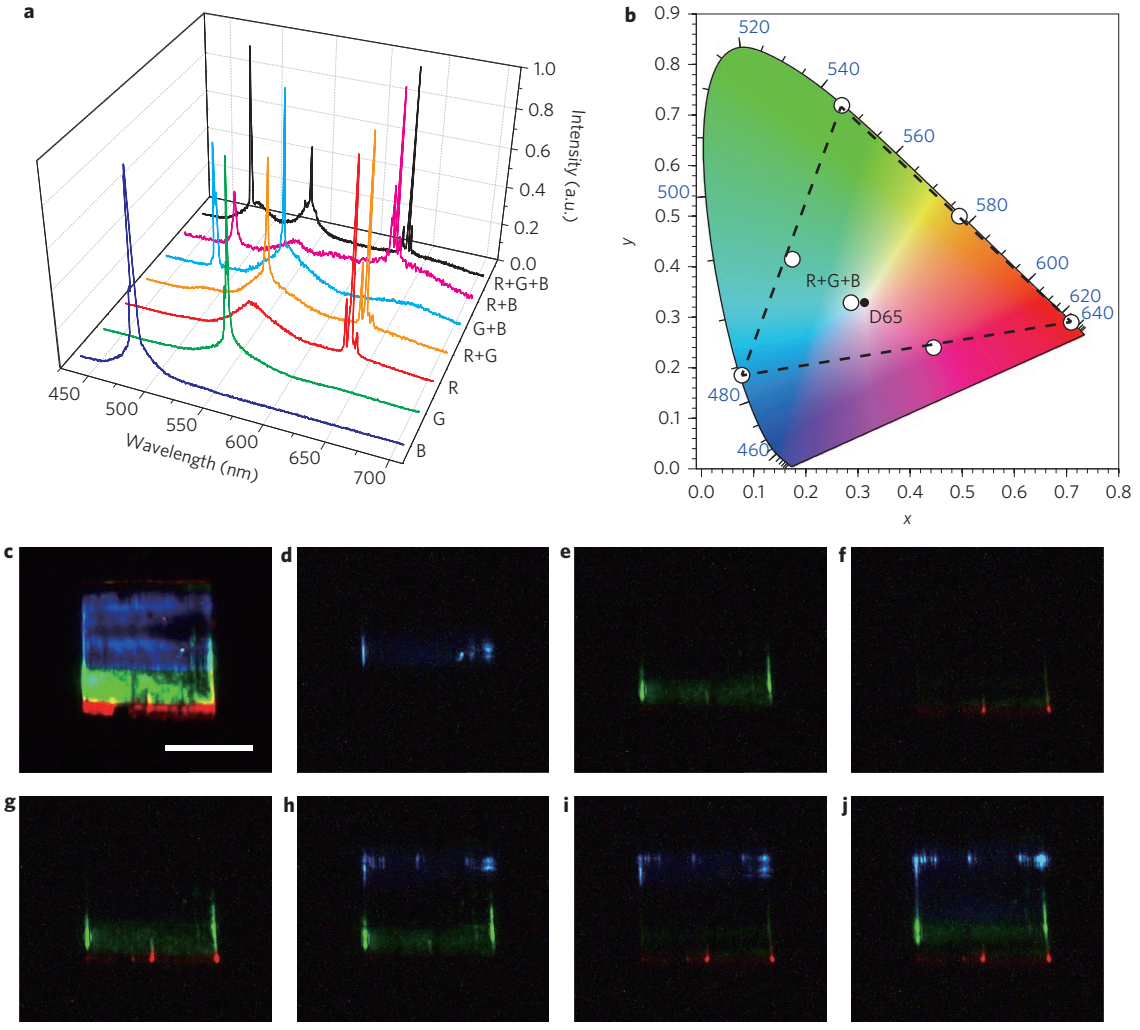

Figure 5 | White and full-colour tunable lasing. a, Lasing spectra when the blue (B), green (G), red (R), red and green (R+G), green and blue (G+B), red and blue (R+B) and red, green and blue (R+G+B) segments are pumped above their respective thresholds. **b**, Chromaticity of the lasing peaks extracted from the spectra in **a**, shown as seven white circles (see Supplementary Section 11 for details of the chromaticity calculation.) The chromaticity of the R+G+B lasing is close to the CIE standard white illuminant D65. Dashed lines indicate the range of the achievable colour gamut for this particular heterostructure. **c**–**j**, Real colour images under low pumping (**c**) and above-threshold pumping (**d**–**j**) for the various colour cases corresponding to the seven spectra in **a**. Scale bar, 20 μm.

scattering from the edges and an additional strong line in the middle of the nanosheet across the green- and light-red-emitting segments due to a bent edge created during transfer of the nanosheet. There is also weaker scattering of the emission due to surface corrugation, which is discussed in detail in Supplementary Section 13. Figure 3c shows the emission at 4.0 μJ pulse energy. It is clear that the uniform emission has been replaced by more pronounced scattering lines and a significantly diminished background, indicating that the transition from spontaneous emission to lasing has occurred. The spectral evolution with increasing pulse energy is shown in Fig. 3d. At the lowest pumping energy of 1.3 μJ, only broadband spontaneous emission is observed. On increasing the pumping energy from 1.8 μJ to 3.3 μJ, narrow peaks at red (642 nm and 675 nm), green (530 nm) and blue (484 nm) colours appear sequentially. Both the intensity and the number of peaks of each colour increase with pumping energy, which can be attributed to well-known multimode lasing behaviour[44]. A lasing wavelength span of 191 nm, much larger than the gain bandwidth of any reported monolithic semiconductor, can be observed. The light-red lasing (642 nm) was generated from the cation-terminated growth front and appears as the red-emitting segment in Fig. 3b,c. The deep-red lasing (675 nm) was generated from the anion-terminated growth front on the opposite side of the nanosheet, which is not visible in Fig. 3b,c because of the weak response of our camera at 675 nm (see the Infinity2-1R Camera Datasheet at http://www.lumenera.com/). Due to the large size of the nanosheet structures, different longitudinal and transverse modes cause very close mode spacing[24], so more modes are excited above the threshold with increasing pumping intensity. At a pumping level of 3.9 μJ, multimode lasing can be clearly observed. High-resolution photoluminescence measurements (Supplementary Fig. 13 and Supplementary Section 10) reveal that the linewidth of each individual mode narrows down to ~0.4 nm once pumped above the lasing threshold.

Further evidence for multi-colour lasing behaviour can be seen for each of the four colours in Fig. 3d in the light-in–light-out curves plotted in Fig. 4a–d, together with theoretical fittings based on multimode lasing equations[45]. Typical S-like curves covering the three regimes of operation are clear in the double-log-scale plots. For all four colours, both the spontaneous emission regime, dominating at lower pumping intensity, and the stimulated emission regime, dominating at higher pumping intensity, have slopes of ~1. The maximum slope of the superlinear transition regime, in which amplified spontaneous emission is the dominant process, varies by colour. These transition slopes are 2.1, 7.3, 2.7 and 2.2 for blue, green, light red and deep red, respectively. Because the maximum slope of the superlinear regime represents the most dramatic transition from spontaneous emission to lasing, this is often used to define the lasing threshold. Based on the four individual light-in–light-out plots, the thresholds for blue, green, light red and deep red lasing are 3.3, 2.9, 2.0 and 3.0 μJ, respectively, for single pulse excitation, corresponding to power densities of 1,441, 1,266, 873 and 1,310 kW cm^{-2}, respectively. A more detailed study of the lasing threshold, output power, lasing efficiency and stability of our multi-segment heterostructure nanosheets is provided in Supplementary Sections 17, 15 and 19.

Full-colour range tuning and white lasing

To illustrate the potential of our multi-segment heterostructure nanosheet for general illumination, we studied dynamic tuning of the mixed colours in the full-colour range and white colour lasing in particular. Three beams were focused into long, narrow, parallel stripes (Supplementary Fig. 11b, Supplementary Section 9) to pump one of the three segments each. The power of each pumping beam could be adjusted independently to allow for precise, independent tuning of the lasing intensity of each colour. As a result, the mixed lasing colours in the far field can be controllably varied in the full-colour range and the desired white colour can be achieved. The results are summarized in Fig. 5, with the photoluminescence image and the structure of the nanosheet shown in Fig. 5c. By pumping one, two and all three of the segments above their lasing thresholds, we demonstrate independent lasing of each RGB colour, simultaneous two-colour lasing of any two of the three primary colours, and finally simultaneous RGB lasing (shown in Fig. 5d–j). Figure 5a presents the emission spectra for all seven cases, while Fig. 5b shows the calculated chromaticity for these lasing spectra on a CIE1931 colour diagram (red, green, blue, magenta, yellow, cyan and white, respectively; Supplementary Section 11). The chromaticity of the carefully balanced white lasing is very close to that of the white point CIE standard white illuminant D65[46] (shown in Fig. 5b). In addition, according to Grassmann's law, all colours inside the triangle formed by the three elementary colours can be realized through appropriate mixing of three colours. One of our best samples (sample #4, Supplementary Section 12) can cover 70% more perceptible colours than the standard RGB[47] space after converting to a perceptually uniform colour space (Supplementary Section 12 and Supplementary Fig.15). Such a large colour gamut, enabled by the flexibility of our approach, could be used in the production of high-contrast-ratio displays with better colour saturation than is available today.

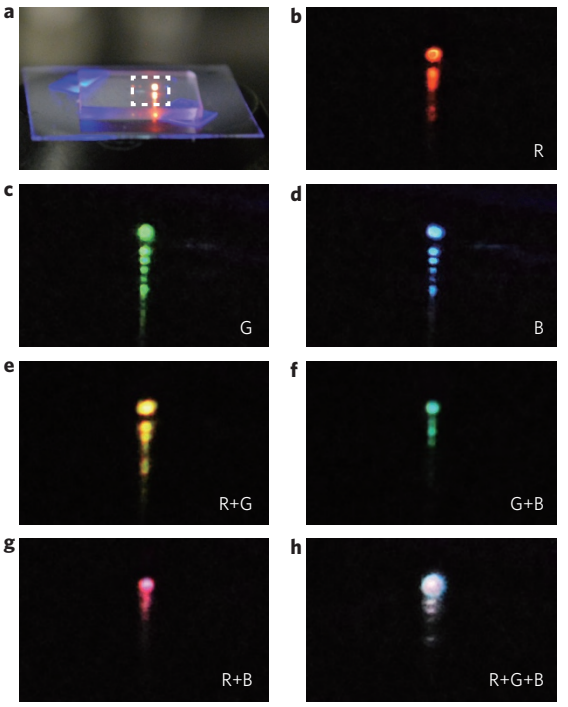

Figure 6 | Colour photographs. a, Photograph of the mixed emission colour from a multi-segment heterostructure nanosheet. (Note that the blue emission visible is from the adhesive between the MgF_2 substrate and the glass slide.) **b**–**h**, Photographs of the enlarged dashed-box region in **a** when the different combinations of segments are pumped as indicated by the labels inside each figure, creating the mixed far-field emission colours red, green, blue, yellow, cyan, magenta and white. The top dots in each photograph are the direct image of laser emission, while the tails under these dots are the reflection from the substrate.

To show the far-field mixing of colours from our multi-colour lasers, real colour photographs were taken (Fig. 6) of the laser output while using dynamic differential pumping (corresponding to the cases of Fig. 5) to control the lasing colour. Figure 6b–d shows independent red, green and blue lasing achieved by pumping each colour segment individually. Yellow, cyan and

magenta mixed lasing emissions were produced by pumping two of the segments, as shown in Fig. 6e–g. Finally, with three beams pumping all three colour segments, simultaneous RGB lasing emission from a single multi-segment heterostructure nanosheet can be mixed together to render as a white-like colour, as shown in Fig. 6h. This colour mixing demonstration provides an experimental proof-of-concept for the use of our multi-colour lasing structure in illumination and display applications.

Conclusions

We have demonstrated simultaneous RGB lasing from individual monolithic ZnCdSSe nanosheets at room temperature. White and tunable lasing over the full range of visible colours has been achieved through controlled pumping of different segments in a multi-segment heterostructure nanosheet of ZnCdSSe quaternary alloys. The key to our successful demonstration lies in the development of a unique growth strategy that exploits the interplay of the VLS, VS and dual-ion exchange mechanisms. Through a detailed characterization and understanding of this growth mechanism, we have designed an optimized growth sequence for each segment, allowing for the growth of nanosheets composed of several parallel segments with the desired alloy compositions, geometry and crystal quality. The parallel cavity arrangement significantly reduces the absorption of shorter-wavelength photons by the narrower-bandgap material when compared with composition-graded one-dimensional nanostructures[25]. As a result, lasing over a wavelength range of 191 nm in a single monolithic structure, the largest ever reported, has been observed. Finally, it is important to note that the term 'white laser', which associates concepts linked to broadband and monochromatic emission, might at first appear self-contradictory. Our results demonstrate that the apparently contradictory terms 'white' and 'lasing' can both be realized in a single monolithic structure. Our work greatly simplifies the process of creating monolithic laser structures with dynamically colour-controllable emissions, and is an important first step towards the realization of an electrically driven white-colour and full-colour nanolaser from a single monolithic structure.

Methods

Methods and any associated references are available in the online version of the paper.

Received 23 October 2014; accepted 15 June 2015;
published online 27 July 2015

References

1. Qian, F. *et al.* Multi-quantum-well nanowire heterostructures for wavelength-controlled lasers. *Nature* **7,** 701–706 (2008).
2. Dang, C. *et al.* Red, green and blue lasing enabled by single-exciton gain in colloidal quantum dot films. *Nature Nanotech.* **7,** 335–339 (2012).
3. Hu, X. P. *et al.* High-power red-green-blue laser light source based on intermittent oscillating dual-wavelength Nd:YAG laser with a cascaded $LiTaO_3$ superlattice. *Opt. Lett.* **33,** 408–410 (2008).
4. Fujimoto, Y., Ishii, O. & Yamazaki, M. Multi-color laser oscillation in Pr^{3+} doped fluoro-aluminate glass fiber pumped by 442.6 nm GaN–semiconductor laser. *Electron. Lett.* **45,** 1301–1302 (2009).
5. Yamashita, K., Takeuchi, N., Oe, K. & Yanagi, H. Simultaneous RGB lasing from a single-chip polymer device. *Opt. Lett.* **35,** 2451–2453 (2010).
6. Tang, S. K. Y. *et al.* A multi-color fast-switching microfluidic droplet dye laser. *Lab Chip* **9,** 2767–2771 (2009).
7. Ding, Y. *et al.* Nanowires/micorfibre hybrid structure multicolor laser. *Opt. Express* **17,** 21813–21818 (2009).
8. Chen, S., Zhao, X., Wang, Y., Shi, J. & Liu, D. White light emission with red-green-blue lasing action in a disordered system of nanoparticles. *Appl. Phys. Lett.* **101,** 123508 (2012).
9. Naderi, N. A. *et al.* Two-color multi-section quantum dot distributed feedback laser. *Opt. Express* **18,** 27026–27035 (2010).
10. Neumann, A. *et al.* Four-color laser white illuminant demonstrating high color-rendering quality. *Opt. Express* **19,** A982–A990 (2011).
11. Wierer, Jr. J. J., Tsao, J. Y. & Sizov, D. S. Comparison between blue laser and light-emitting diodes for future solid-state lighting. *Laser Photon. Rev.* **7,** 963–993 (2013).
12. Zhao, J., Jiang, H. & Di, J. Recording and reconstruction of a color holographic image by using digital lensless Fourier transform holography. *Opt. Express* **16,** 2514–2519 (2008).
13. Chellappan, K., Erden, E. & Urey, H. Laser-based displays: a review. *Appl. Opt.* **49,** F79–F98 (2010).
14. Kotani, A. *et al.* EndoV/DNA ligase mutation scanning assay using microchip capillary electrophoresis and dual-color laser-induced fluorescence detection. *Anal. Methods* **4,** 58–64 (2012).
15. Pascu, M. L., Moise, N. & Staicu, A. Tunable dye laser applications in environment pollution monitoring. *J. Mol. Struct.* **598,** 57–64 (2001).
16. Lin, W. Y. *et al.* 410 m/500 Mbps WDM visible light communication systems. *Opt. Express* **20,** 9919–9924 (2012).
17. Cossu, G., Khalid, A. M., Choudhury, P., Corsini, R. & Ciaramella, E. 3.4 Gbit/s visible optical wireless transmission based on RGB LED. *Opt. Express* **20,** B501–B506 (2012).
18. Alivisatos, A. P. Semiconductor clusters, nanocrystals, and quantum dots. *Science* **271,** 933–937 (1996).
19. Huang, Y., Duan, X. F. & Lieber, C. M. Nanowires for integrated multicolor nanophotonics. *Small* **1,** 142–147 (2005).
20. Kuykendall, T., Ulrich, P., Aloni, S. & Yang, P. Complete composition tunability of InGaN nanowires using a combinatorial approach. *Nature Mater.* **6,** 951–956 (2007).
21. Yang, Z. *et al.* On-nanowire spatial band gap design for white light emission. *Nano Lett.* **11,** 5085–5089 (2011).
22. Anikeeva, P. O., Halpert, J. E., Bawendi, M. G. & Bulovic, V. Quantum dot light-emitting devices with electroluminescence tunable over the entire visible spectrum. *Nano Lett.* **9,** 2532–2536 (2009).
23. Kim, T. *et al.* Full-colour quantum dot displays fabricated by transfer printing. *Nature Photon.* **5,** 176–182 (2011).
24. Fan, F. *et al.* Simultaneous two-color lasing in a single CdSSe heterostructure nanosheet. *Semicond. Sci. Technol.* **28,** 065005 (2013).
25. Liu, Z. *et al.* Dynamical color-controllable lasing with extremely wide tuning range from red to green in a single alloy nanowire using nanoscale manipulation. *Nano Lett.* **13,** 4945–4950 (2013).
26. Kim, Y. L. *et al.* CdS/CdSe lateral heterostructure nanobelts by a two-step physical vapor transport method. *Nanotechnology* **21,** 145602 (2010).
27. VEM. *Thin Film Evaporation Guide* (Lebow Corporation and Vacuum Engineering & Materials Inc., 2008).
28. Fang, X. *et al.* ZnS nanostructures: from synthesis to applications. *Prog. Mater. Sci.* **56,** 175–287 (2011).
29. Yue, G. H. *et al.* Synthesis of two-dimensional micron-sized single-crystalline ZnS thin nanosheets and their photoluminescence properties. *J. Cryst. Growth.* **293,** 428–432 (2006).
30. Moore, D. & Wang, Z. L. Growth of anisotropic one-dimensional ZnS nanostructures. *J. Mater. Chem.* **16,** 3898–3905 (2006).
31. Ding, J. X. *et al.* Lasing in ZnS nanowires grown on anodic aluminum oxide templates. *Appl. Phys. Lett.* **85,** 2361–2363 (2004).
32. Liu, Y. *et al.* Wavelength-controlled lasing in $Zn_xCd_{1-x}S$ single-crystal nanoribbons. *Adv. Mater.* **17,** 1372–1377 (2005).
33. Pan, A. L., Liu, R. B., Sun, M. H. & Ning, C. Z. Quaternary alloy semiconductor nanobelts with bandgap spanning the entire visible spectrum. *J. Am. Chem. Soc.* **131,** 9502–9503 (2009).
34. Pan, A. *et al.* Continuous alloy-composition spatial grading and superbroad wavelength-tunable nanowire lasers on a single chip. *Nano Lett.* **9,** 784–788 (2009).
35. Dloczik, L. & Konenkamp, R. Nanostructure transfer in semiconductors by ion exchange. *Nano Lett.* **3,** 651–653 (2003).
36. Son, H. D., Hughes, M. S., Yin, Y. & Alivisatos, P. A. Cation exchange reactions in ionic nanocrystals. *Science* **306,** 1009 (2004).
37. Moon, D. G. *et al.* Chemical transformations of nanostructured materials. *Nano Today* **6,** 186–203 (2011).
38. Wang, Y. *et al.* Gas-phase anion exchange towards ZnO/ZnSe heterostructures with intensive visible light emission. *J. Mater. Chem. C* **2,** 2793–2798 (2014).
39. Deng, Z., Yan, H. & Liu, Y. Band gap engineering of quaternary-alloyed ZnCdSSe quantum dots via a facile phosphine-free colloidal method. *J. Am. Chem. Soc.* **131,** 17744–17745 (2009).
40. Ichino, K., Onishi, T., Kawakami, Y., Fujita, S. & Fujita, S. Growth of ZnS and ZnCdSSe alloys on GaP using an elemental sulfur source by molecular beam epitaxy. *J. Cryst. Growth.* **138,** 28–34 (1994).
41. Wang, Z. Y., Lu, Q. F., Fang, X. S., Tian, X. K. & Zhang, L. D. Manipulation of the morphology of CdSe nanostructures: the effect of Si. *Adv. Funct. Mater.* **16,** 661–666 (2006).
42. Wang, M. & Fei, G. T. Synthesis of tapered CdS nanobelts and CdSe nanowires with good optical property by hydrogen-assisted thermal evaporation. *Nanoscale Res. Lett.* **4,** 1166–1170 (2009).

43. Tong, L. M. *et al.* Assembly of silica nanowires on silica aerogels for microphotonic devices. *Nano Lett.* **5,** 259–262 (2005).
44. Zimmler, M. A., Capasso, F., Muller, S. & Ronning, C. Optically pumped nanowire lasers: invited review. *Semicond. Sci. Technol.* **25,** 024001 (2010).
45. Casperson, L. W. Threshold characteristics of multimode laser oscillators. *J. Appl. Phys.* **46,** 5194–5201 (1975).
46. International Commission on Illumination. *CIE 15 Colorimetry Technical Report*, 3rd edn, US Government Document (International Commission on Illumination, 2004).
47. International Electrotechnical Commission. *Multimedia Systems and Equipment—Colour Measurement and Management—Part 2-1 Colour Management—Default RGB Colour Space–sRGB*, IEC 61966-2-1 (International Electrotechnical Commission, 1999).

Acknowledgements

The authors thank the Army Research Office for their initial support on nanowire research (award no. W911NF-08-1-0471, under M. Gerhold) that eventually led to this work. The authors acknowledge the use of facilities within the LeRoy Eyring Center for Solid State Science at Arizona State University, especially D. Wright and A.J. Mardinly for their assistance with the CVD set-up and high-resolution TEM, respectively. F.F. thanks the China Scholar Council for a scholarship, and S.T. thanks the Republic of Turkey's Ministry of National Education for financial support through its fellowship.

Author contributions

C.Z.N. created the concept, initiated the research on the white lasers, and supervised the overall project. S.T. developed the growth strategy and was responsible for the growth of multi-segment heterostructure nanosheets and the structural and chemical characterizations. F.F. and Z.L. designed and performed the key optical experiments, theoretical calculations and simulations. D.S. carried out the AFM measurements, as well as other optical measurements. All authors participated in regular data analysis, discussed the research results, and were involved in the preparation and various revisions of the manuscript.

Additional information

Supplementary information is available in the online version of the paper. Reprints and permissions information is available online at www.nature.com/reprints. Correspondence and requests for materials should be addressed to C.Z.N.

Competing financial interests

The authors declare no competing financial interests.

Methods

Sample synthesis. Multi-segment heterostructure nanosheets (MSHNs) were grown on a SiO_2/Si substrate by a combination of VLS, VS and dual-ion exchange growth mechanisms using a single zone CVD horizontal tube (1.5 inches wide, 4 foot long) reactor. The substrate serves only as a mechanical support. MSHNs are otherwise grown as freestanding structures without epitaxial connection with the substrate, because the original growth substrates can be amorphous or non-lattice-matched crystals. The overall set-up and VLS growth mechanism are described in several earlier papers[24,33,48] and are shown schematically in Fig. 1a. CdSe and ZnS powders (Sigma Aldrich, 99.99% metal basis) were used as source materials. Specific details that are new to the present paper are described in Fig. 1 and in Supplementary Section 5. Before growth, the SiO_2/Si substrate was cleaned and then coated with a 10 nm layer of sputtered Au. After placing ZnS (at the centre, $T = 980$ °C), CdSe (12 cm upstream from the centre, $T \approx 840$ °C) and the substrate (16 cm downstream from the centre, $T \approx 640$ °C) inside the reactor, as shown in Fig. 1, the system was evacuated to 30 mtorr. A 10 s.c.c.m. N_2 inert gas flow was introduced for 30 min to purge the reactor of O_2. The system pressure was then set to 10 torr with backfilled N_2 and the furnace was turned on. After completion of the growth, the furnace was turned off and allowed to cool naturally to room temperature while continuing the 10 s.c.c.m. N_2 flow. The growth time in each step of the experiment was shorter than 12 min to prevent source depletion.

Material characterization. Structural characterization of the MSHNs was carried out using a JEOL 2010F TEM equipped with a Link energy-dispersive X-ray spectroscopy detector at 200 kV and an FEI XL30 environmental SEM at 15 kV. It is worth noting that the sample used for TEM characterization was deliberately chosen from a broken nanosheet piece to eliminate bending during dispersion onto the TEM grid, which would introduce difficulty in finding the zone axis. As-grown structures were dispersed onto a glass substrate via contact-printing[49] and then moved to a TEM grid using a homemade tapered fibre. Surface characterization was performed with a Bruker Dimension 3000 atomic force microscope (AFM) in tapping mode using a standard pyramidal SiN tip at a scan rate of 0.5 Hz. This set-up provides a Z-resolution of ~0.07 nm.

Optical measurements. Samples were first cleaved from as-grown pieces by the bend-to-fracture method[43]. High-quality end facets were thus created as partially reflective mirrors to define the laser cavities. All optical measurements were performed at room temperature. After the fracture, samples were then transferred individually onto MgF_2 substrates (refractive index of ~1.38) for enhanced optical confinement using a homemade tapered fibre. In the single-beam uniform pumping experiment (schematically shown in Supplementary Fig. 11a) for the multi-colour lasing shown in Figs 3 and 4, the third harmonic of a Q-switched Nd: YAG laser (Spectra Physics) was used to uniformly pump the individual samples ($\lambda = 355$ nm, repetition rate of 10 Hz, pulse width of 9 ns) at an angle of 15° from the sample normal, with a spot size of 180 μm. The resulting emission was collected through a dark-field objective lens (Olympus LMPlanLF ×50, numerical aperture of 0.5) at an angle of 45° from the sample normal to enhance the collection efficiency of stimulated emission and reduce the spontaneous emission background. The collected light was then directed though a beamsplitter and gathered simultaneously by a charge-coupled device (CCD) camera (Lumenera Infinity 2-1R) and monochromator (Triax 320) equipped with a Si array detector (Jobin Yvon CCD). A long-wavelength-pass 405 filter (Semrock EdgeBasic) was used to remove the pump laser wavelength from the collected spectra. In the lasing colour tuning and mixing experiments shown in Figs 5 and 6, the third harmonic of a Q-switched Nd: YLF laser (Spectra Physics, $\lambda = 349$ nm, repetition rate of 10 Hz, pulse width of 5 ns) was used to provide better pulse-to-pulse stability. Details of the set-up are shown in Supplementary Fig. 11b. The laser was first directed through a set of cylindrical lenses to change the length-to-width ratio of the laser spot. After splitting into three separate beams, each beam was then directed through three independent polarizer and analyser set-ups and focused to a 260 μm × 5 μm narrow stripe-like spot parallel to the cavity length direction. The same collection set-up was used for photoluminescence images and spectra recording, with only the collection angle of the objective being changed. An additional CCD camera (Nikon D60) was used to take ×1 magnification photographs to demonstrate the far-field colour mixing. The laser pump angle, objective collection angle and camera collection angle were 60°, 0° and 75°, respectively, from the sample normal (for detailed optical set-up information see Supplementary Section 9).

References

48. Pan, A., Liu, R., Sun, M. & Ning, C. Z. Spatial composition grading of quaternary ZnCdSSe alloy nanowires with tunable light emission between 350 and 710 nm on a single substrate. *ACS Nano* **4,** 671–680 (2010).
49. Fan, Z. *et al.* Wafer-scale assembly of highly ordered semiconductor nanowire arrays by contact printing. *Nano Lett.* **8,** 20–25 (2008).